

## A new type of spherical flexure joint based on tetrahedron elements

Rommers, Jelle; van der Wijk, Volkert; Herder, Just L.

**DOI**

[10.1016/j.precisioneng.2021.03.002](https://doi.org/10.1016/j.precisioneng.2021.03.002)

**Publication date**

2021

**Document Version**

Final published version

**Published in**

Precision Engineering

**Citation (APA)**

Rommers, J., van der Wijk, V., & Herder, J. L. (2021). A new type of spherical flexure joint based on tetrahedron elements. *Precision Engineering*, 71, 130-140.  
<https://doi.org/10.1016/j.precisioneng.2021.03.002>

**Important note**

To cite this publication, please use the final published version (if applicable).  
Please check the document version above.

**Copyright**

Other than for strictly personal use, it is not permitted to download, forward or distribute the text or part of it, without the consent of the author(s) and/or copyright holder(s), unless the work is under an open content license such as Creative Commons.

**Takedown policy**

Please contact us and provide details if you believe this document breaches copyrights.  
We will remove access to the work immediately and investigate your claim.



# A new type of spherical flexure joint based on tetrahedron elements

Jelle Rommers<sup>\*</sup>, Volkert van der Wijk, Just L. Herder

Department of Precision and Microsystems Engineering, Faculty of 3mE, Delft University of Technology, Delft, the Netherlands

## ARTICLE INFO

### Keywords:

Flexure  
Compliant mechanism  
Spherical joint  
Planar joint  
Tetrahedron

## ABSTRACT

In this paper we present two new designs of spherical flexure joints, which are the compliant equivalent of a traditional ball-and-socket joint. The designs are formed by tetrahedron-shaped elements, each composed of three blade flexures with a trapezoidal shape, that are connected in series without intermediate bodies. This is new with respect to the designs currently found in literature and helps to increase the range of motion. We also present two planar ( $x$ - $y$ - $\theta_z$ ) flexure joint designs which were derived as special versions of the spherical designs. In these designs the tetrahedron elements have degenerated to a triangular prisms. For detailed investigation we developed equivalent representations of the tetrahedron and triangular prism elements and proved that three of the four constraint stiffness terms depend solely on the properties of the main blade flexure. Furthermore, we derived equations for these stiffness terms which are compared to finite-element simulations, showing a good correspondence for the prism element with a Normalized Mean Absolute Error (NMAE) of 1.9%. For the tetrahedron element, the equations showed to only capture the qualitative behaviour with a NMAE of 34.9%. Also, we derived an equation for the optimal width of the prism element regarding rotational stiffness.

## 1. Introduction

Spherical flexure joints can provide a high-precision alternative for traditional ball-and-socket joints. This is because they gain their motion due to the deflection of slender segments such as thin spring steel plates, which eliminates friction and backlash in the rolling and sliding surfaces in these traditional joints. Four types of spherical flexure joint designs can currently be distinguished in literature [1], all allowing solely three rotations in a single point.

The first type consists of a rod with a thinner part or short wire as illustrated in Fig. 1a [2], which allows solely three rotations because all strains are concentrated in the thinner part. The second type consists of three wire flexures or slender rods which intersect in a common point as shown in Fig. 1b [3,4], where each wire flexure constrains one translational motion. The third design type is based on the traditional (rigid-body) spherical linkage in which the axes of three revolute joints intersect in a single point. The revolute joints have been replaced by a flexure-based counterpart for which there are various possibilities, for example as illustrated in Fig. 1c [5,6]. The fourth type shown in Fig. 1d can be regarded as the design of Fig. 1b with the wire flexures replaced with ‘folded leaf springs’ [1,3,7], which each also constrains one translational motion [3].

The second, third and fourth design types have special configurations

where they degenerate to planar joints which allow two in-plane translations and one rotation. For example in design type two in Fig. 1b, where the length axes of the wire flexures intersect in the rotation point  $P$ . If point  $P$  is shifted to infinity in the vertical direction, the wire flexures become parallel and a planar joint results. In a similar way, design type four shown in Fig. 1d degenerates into a planar joint when the fold lines of the folded leaf springs become parallel. The third design type shown in Fig. 1c also has a planar version which consists of two links and three revolute flexure joints with parallel rotation axes.

In this paper, we present a new type of spherical flexure joint which is formed by a serial connection of tetrahedron-shaped elements. We present two design variations named the Tetra I and Tetra II, and also present their planar derivatives in which the tetrahedron elements degenerate into triangular prisms. We have published one of these planar versions in earlier work [8] where the triangular prism was inspired by the ‘infinity hinge’ from Refs. [9,10]. In this paper we show that the tetrahedron element is a generalized version of the triangular prism.

In section 2 we present the joint designs and explain how they function. The tetrahedron element is studied in detail in section 3 by means of an equivalent representation. Equations for the stiffness terms are derived and compared to finite-element simulations. In section 4 we discuss the results and in section 5 we summarize the contributions of

<sup>\*</sup> Corresponding author.

E-mail address: [j.rommers@tudelft.nl](mailto:j.rommers@tudelft.nl) (J. Rommers).

this work.

Throughout the article, we refer to motions of a body as being *free* when a significantly low stiffness is being experienced in that direction, and as *constrained* in the case of a significantly high stiffness. A flexure typically adds *constraints* to a body, meaning that it stiffens certain motion directions of the body [11].

## 2. Designs of the two new spherical flexure joints and their planar derivatives

In this section we first present the designs of two new spherical flexure joints and subsequently we present their planar derivatives. The designs consist of tetrahedron elements connected in series. In the first design, the elements are connected along two arms as illustrated in Fig. 2, while in the second design the elements form a nested configuration as illustrated in Fig. 5.

The first design, named Tetra I, is shown in Fig. 2a. It can be considered as consisting of two arms, each built up from four tetrahedron elements and with  $e$  as the end-effector. For illustration, in  $e$  a rod is placed which ends in point  $P$ , the remote center of rotation of the flexure joint which floats in space. The flexures constrain the end effector  $e$  such that solely the three rotations about point  $P$  are free. If, for example, a horizontal force is applied at the top of the joint in  $e$ , the joint rotates about point  $P$  as shown in the two deformed states (scaled 1:1) in Fig. 3.

The working principle of the Tetra I design is as follows. The two arms each consist of four tetrahedron elements. A single tetrahedron element, shown isolated in Fig. 4, consists of three blade flexures  $ac$ ,  $ab$  and  $bc$ . Edges  $a_1a_3$  and  $c_1c_3$  are the interfaces at which other tetrahedron elements can be connected and therefore blade flexure  $ac$  is considered as the main (connecting) blade flexure. In the isolated view, we consider edge  $a_1a_3$  as fixed and the rigid bar through edge  $c_1c_3$  as the end effector. The three blade flexures have a trapezoidal shape and the lines through their edges form a tetrahedron shape, as illustrated in Fig. 4. Coordinate system  $xyz$  is placed with its origin at point  $a_1$ . Axis  $x$  is aligned with line  $a_1c_1$  and axis  $y$  is in the plane formed by points  $a_1b_1c_1$ . Coordinate system  $uvw$  has the same orientation as system  $xyz$ , except that it is rotated around the  $x$ -axis such that  $v$  is perpendicular to the plane of blade flexure  $ac$ . The rigid bar is free to rotate around the axes  $u$  and  $w$ , which lie in the plane of blade flexure  $ac$ . This is because the planes formed by the three blade flexures intersect in point  $P$ , as will be explained in more detail in section 3.2. In order to achieve spherical motion, rotation around the third axis  $v$  perpendicular to the plane of blade flexure  $ac$  should also be free. This is accomplished by connecting a second tetrahedron under an angle with respect to the first tetrahedron, such that the main blade flexures of the two tetrahedron elements are not coincident. For example, the fourth and fifth tetrahedron of the Tetra I design shown in Fig. 2a are connected under an angle with respect to each other in order to free the rotation around the third axis. The tetrahedron elements should be connected such that their rotation points coincide, which means that the planes of all blade flexures in the spherical joints intersect point  $P$ . In principle, the spherical flexure joint design needs solely two tetrahedrons under an angle to function properly. However,

each of the tetrahedrons can also be replaced by a set of tetrahedrons in series in order to increase the range of motion and to avoid collisions, such as in the Tetra I design in Fig. 2a which consists of four tetrahedrons in each arm, paired two by two on each side.

The second new design of a spherical flexure joint named Tetra II is shown in Fig. 5a. This design also consists of tetrahedron elements, however assembled in a nested configuration. The tetrahedron elements are constructed in series, similar as in the Tetra I design in which the two arms are formed by a serial connection of tetrahedron elements. Also in the Tetra II design, point  $P$  is the remote center of rotation. If, for example, a horizontal force is applied at point  $e$ , the joint rotates about  $P$  as shown in the deformed state (scaled 1:1) in Fig. 5b. A movie of this design can be found online using the DOI of this article, in which the motions of an additively manufactured titanium version are demonstrated. Two tetrahedron elements connected under an angle are sufficient for spherical motion, while the third element was added to improve the range of motion. Note that the three tetrahedron elements not only differ in size, but also in shape. This is different from the Tetra I design, where all tetrahedron elements have the same shape and size. Changing the shape of the tetrahedron elements does not change the kinematics of the spherical joint, as long as the planes of all three blade flexures forming the tetrahedron elements coincide in point  $P$ . This will be explained in more detail in section 3.2.

Both of the spherical joint designs Tetra I and II in Figs. 2 and 5 have a specific case for which they become planar joints, shown in Fig. 6a and b, respectively. Here the tetrahedron elements have become triangular prism elements as shown in Fig. 4b. The mobility of the end effector  $e$  is no longer spherical. In both designs the end effectors have 3-DoF planar motion capability, with an  $x$ - and  $y$ -translation and an in-plane rotation  $\theta_z$ . The transformation from spherical to planar mobility can be understood as follows. The end effector  $e$  of a spherical joint moves over the surface of a sphere. If the radius of this sphere is infinitely large, the spherical surface degenerates to a plane. This means that the motions of the joint also become planar. A requirement for the planar joints is that the planes of all blade flexures should be parallel to a single axis, as will be explained in more detail in section 3.2. In Ref. [8] we have already shown how planar joint 1 can be applied for the design of a linear guide.

The four joint designs presented in this section are based on distributed compliance, which enables a significant range of motion. Fig. 7 shows a finite-element simulation of planar joint 1, forced in a straight-line motion. The flexures show a gradual curvature, which means that the strains are well distributed over the whole joint. If the prism elements would be solid, high peak stresses would occur in the connection points which would significantly limit the range of motion.

## 3. The tetrahedron and prism elements in detail

At the core of the four presented joints lie the tetrahedron and prism elements, of which we explain the functioning in detail in this section. Using equivalent representations we analyze their degrees of freedom and derive stiffness equations for their constraining directions, which we compare to finite-element simulations. We assume that blade flexures  $ab$

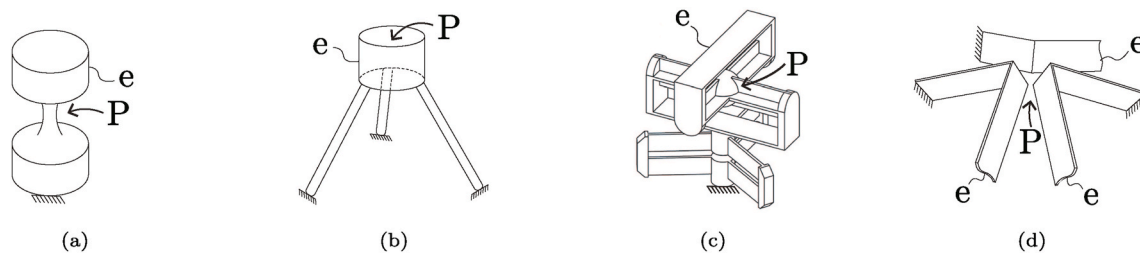


Fig. 1. Overview of the current state-of-the-art spherical flexure joints from Ref. [1], where  $P$  denotes the center of rotation and  $e$  the end effector: (a) a spherical notch joint or short wire flexure [2]; (b) three wire flexures with intersecting axes [3,4]; (c) three revolute flexure joints in series with intersecting motion axes [5,6]; (d) three folded leaf springs with intersecting fold lines [1,3,7].

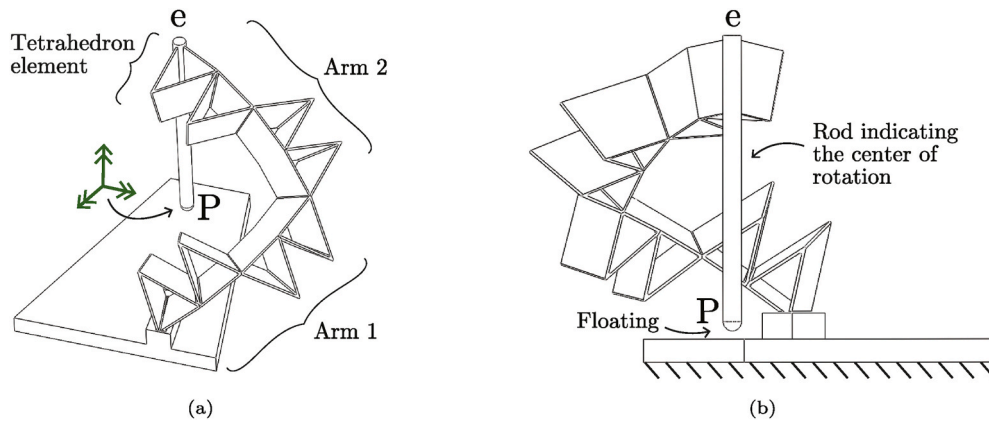


Fig. 2. The Tetra I spherical flexure joint design, shown from two sides, based on two arms under an angle consisting each of four tetrahedron elements. Point P is the remote center of rotation, indicated by the rod eP.

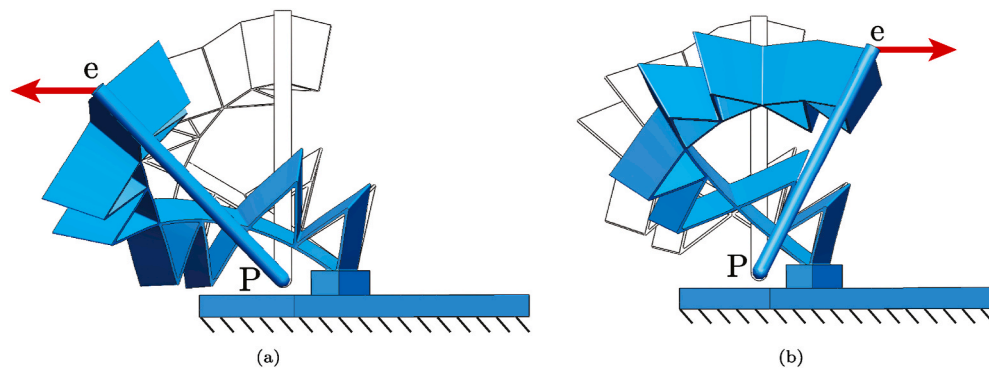


Fig. 3. The Tetra I design subjected to a horizontal load at e, showing that it rotates about point P (scaled 1:1).

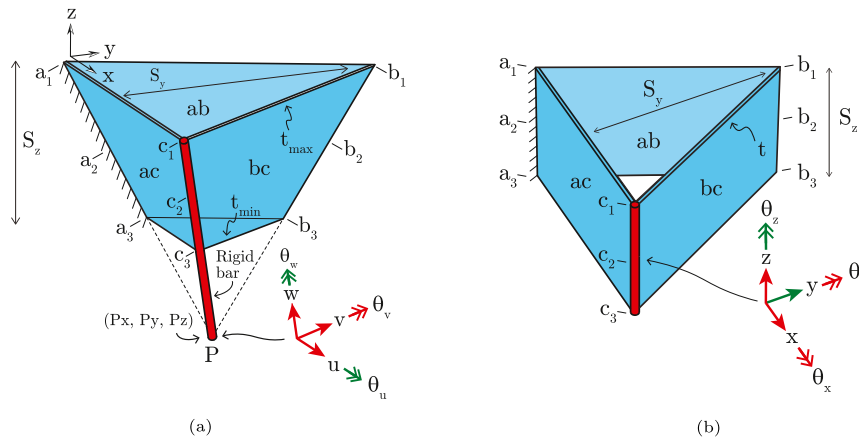


Fig. 4. (a) Tetrahedron element formed by three blade flexures, with its parameters; (b) Specific degenerated case when P lies at infinity, for which the form reduces to a triangular prism.

and  $bc$  have equal lengths, and that for the tetrahedron element  $P_x = L_{a_1c_1}/2$  and  $P_y = 0$ , with  $P_x$  and  $P_y$  the  $x$ - and  $y$ -coordinates of the remote center of rotation as illustrated in Fig. 4a.

### 3.1. Equivalent representations of the tetrahedron and prism elements

Analysis of the tetrahedron and prism elements is not evident because the three blade flexures form a hybrid serial and parallel configuration: blade flexures  $ab$  and  $bc$  form a serial path from ground to the end effector (edge  $c_1c_3$ ), and blade flexure  $ac$  forms a second, parallel

path. It is not directly clear which stiffness blade flexure  $bc$  applies to the end effector because it is connected to the fixed world via blade flexure  $ac$ . The goal of the equivalent representation is to simplify the tetrahedron and prism element such that they consist of two parallel flexure elements. This is done by replacing blade flexures  $ab$  and  $bc$  with a single wire flexure and extending the end effector using a rigid bar, as illustrated in Fig. 8. Points  $a_2$ ,  $b_2$  and  $c_2$  are in the middle of the edges. Edge  $c_1c_3$  in the equivalent mechanism is still the end effector, which is extended such that it forms the rigid part. Two parallel paths are present: the wire flexure and blade flexure  $ab$ . In the following, we explain why

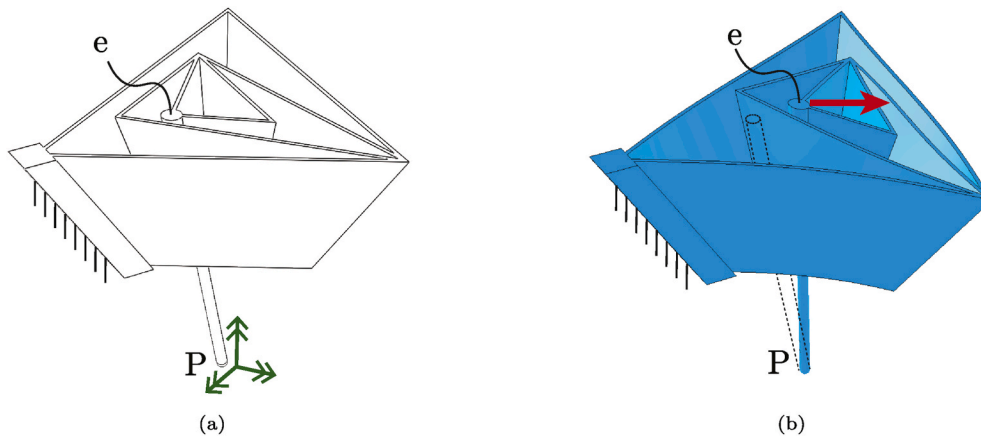


Fig. 5. (a) The Tetra II spherical flexure joint design based on nested tetrahedron elements; (b) Deflected pose due to a load showing the rotational motion about P.

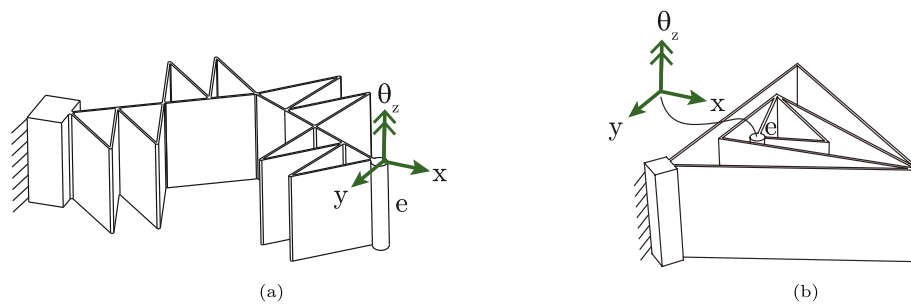


Fig. 6. (a) 3-DoF planar joint 1, derived as special case from the Tetra I design in Fig. 2a; (b) 3-DoF planar joint 2, derived as special case from the Tetra II design in Fig. 5a.

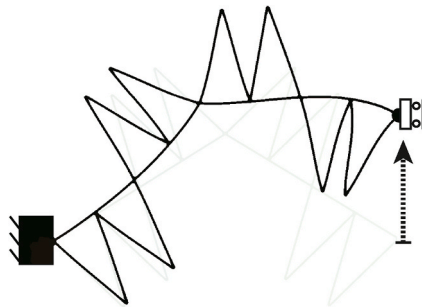


Fig. 7. Illustration of the distributed compliance by a finite-element simulation of planar joint 1 forced in a straight-line motion [8]. The distributed strains enable a large range of motion.

these equivalent representations are valid.

We start with the equivalent representation of the special prism element. Blade flexures  $ab$  and  $bc$  in the original prism element form a folded leaf spring (or double blade flexure), as illustrated in Fig. 9a. An equivalent rigid-body model of this folded leaf spring is illustrated in Fig. 9b, in which the deformation modes with low stiffness are represented by revolute joints connected by rigid bars, as in Ref. [5]. The end effector is extended with a rigid bar which runs to underneath point  $b_2$ . The force  $F_{bp}$  is constrained because it either intersects or is parallel to each of the rotation vectors of the revolute joints [12], such that it does not result in a moment around any of the revolute joints. This is solely the case for forces collinear with the rotation axis of the revolute joint at  $b_2$ . Moments are not counteracted by the folded leaf spring because the rotation vectors of the revolute joints span the full space. A wire flexure coincident with edge  $b_1b_3$  constrains the same motions and is therefore kinematically equivalent to the folded leaf spring. Therefore, the rigid

bar and wire flexure illustrated in Fig. 9c can be used to replace blade flexures  $ab$  and  $bc$ . The same reasoning can be used to explain why the equivalent representation of the tetrahedron is valid. Also in this case, the folded leaf spring formed by blade flexures  $ab$  and  $bc$  of the tetrahedron element solely resists forces collinear with edge  $b_1b_3$ . A wire flexure placed at this edge can replace blade flexures  $ab$  and  $bc$ , as illustrated in Fig. 8a. In earlier work [8], we presented an explanation largely similar to the one in this paragraph. A different explanation can be found in Ref. [13] where instead of adding the free directions of the two blade flexures  $ab$  and  $bc$ , the author analyzes the overlap of their constraints using an ‘intermediate constraint space’.

The equivalent representations in Fig. 8 are only valid for small deflections from the initial shape since the wire flexure suffers from a shortening effect at larger displacements. This shortening does not occur in a folded leaf spring.

### 3.2. Degrees of freedom of the tetrahedron and prism elements

Using the equivalent representations and constraint-based design (CBD) methods [11,12,14], the degrees of freedom of the tetrahedron and prism elements can be understood. We start with the tetrahedron element. Using CBD, the blade flexure  $ac$  is represented by three ‘constraint lines’ running through points  $a_1c_1$ ,  $a_3c_3$  and  $a_1c_3$  in Fig. 8a. A fourth constraint line at the place of the wire flexure represents this element. The CBD methods state that the end effector is solely free to rotate around axes which intersect all constraint lines. This means that the tetrahedron element is solely free to rotate around the axes which lie in the plane of blade flexure  $ac$  and intersect point  $P$ . This results in the two independent rotations around axes  $u$  and  $w$  illustrated in Fig. 4a.

The same method can be applied to the prism element, which is created by shifting the rotation point  $P$  of the tetrahedron element at infinity in the  $z$ -direction. Assume that the first of the two independent

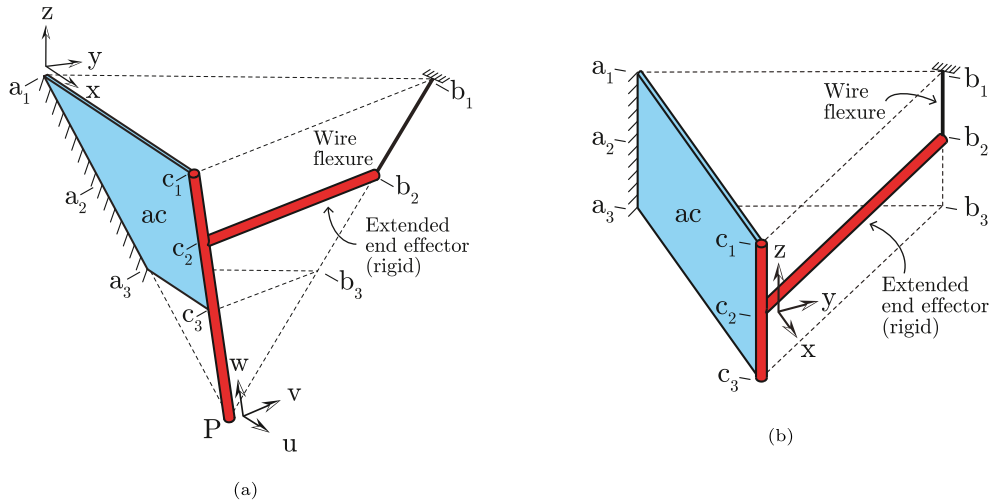


Fig. 8. (a) Equivalent representation of the tetrahedron element where blade flexures  $ab$  and  $bc$  are replaced with a rigid part and a wire flexure; (b) Similar equivalent representation of the prism element.

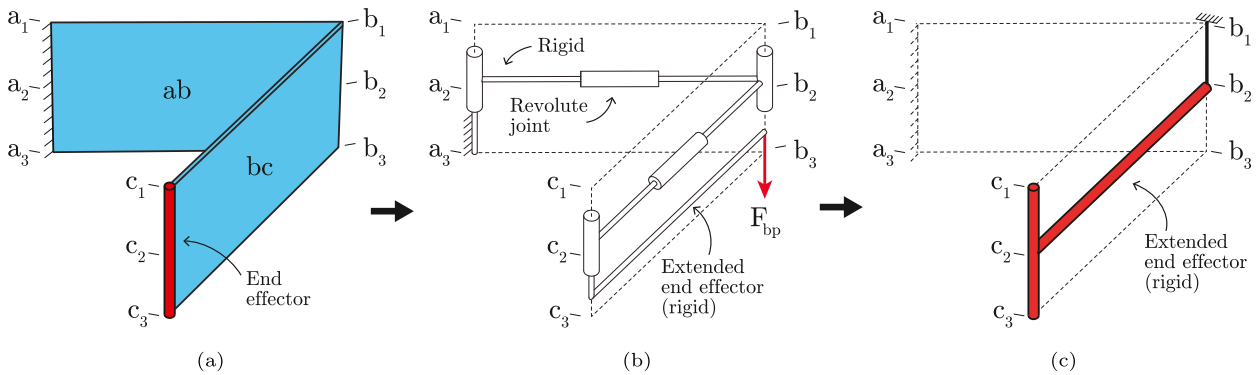


Fig. 9. Blade flexures  $ab$  and  $bc$  of the prism element form a folded leaf spring as illustrated in a), which solely counteracts forces collinear with edge  $b_1b_3$  as shown in the equivalent rigid-body model in b). Therefore, they can be modeled with a wire flexure and rigid bar illustrated in c).

rotation axes of the tetrahedron element is collinear with edge  $c_1c_3$ , and the second one is perpendicular to this edge (but in the plane of blade flexure  $ac$ ). In the prism element, the first axis still intersects all constraint lines because the constraint line representing the wire flexure is intersected at infinity. This means that the prism is free to rotate around the  $y$ -axis in Fig. 8b. The second rotation axis perpendicular to edge  $c_1c_3$  and in the plane of blade flexure  $ac$  lies at infinity because point  $P$  lies at infinity in the  $z$ -direction. This rotation at infinity results in the translational degree of freedom of the prism element in the direction perpendicular to blade flexure  $ac$ . In CBD, this freedom line is represented by a ‘hoop’ in the plane of blade flexure  $ac$ .

### 3.3. Equivalent stiffness of the wire flexure

In order to calculate the stiffness terms of the tetrahedron and prism elements in the next sections, we need to know the longitudinal stiffness of the wire flexure such that it represents the stiffness due to blade flexures  $ab$  and  $bc$ . In the prism element, blade flexures  $ab$  and  $bc$  form a folded leaf spring with parallel edges, of which this stiffness  $K_{bp}$  is given by Ref. [3] using linear beam theory, as:

$$K_{bp} = \left[ \frac{L_{a_2b_2}^3 + L_{b_2c_2}^3}{3EI_p} + \frac{6(L_{a_2b_2} + L_{b_2c_2})}{5Gth} \right]^{-1}, \quad (1)$$

where  $L_{a_2b_2} = \sqrt{L_{a_2c_2}^2/4 + S_y^2}$  is the distance between point  $a_2$  and  $b_2$ , or

the length of blade flexure  $ab$ .  $S_y$  is the width of the total element, which is the dimension in the  $y$ -direction in Fig. 4b.  $E$  and  $G$  are the Young’s modulus and shear modulus, respectively. The area moment of inertia is  $I_p = tS_y^3/12$ , where  $t$  and  $S_y$  are the thickness and height of the blade flexures as indicated in Fig. 4b. The first and second term in brackets in equation (1) describe the displacement due to bending and shear, respectively. Because we assume that the lengths of the blade flexures  $ab$  and  $bc$  are equal,  $L_{a_2b_2} = L_{b_2c_2}$  and equation (1) can be simplified to:

$$K_{bp} = \left[ \frac{2L_{a_2b_2}^3}{3EI_p} + \frac{12L_{a_2b_2}}{5Gth} \right]^{-1}. \quad (2)$$

The equivalent stiffness of the wire flexure for the tetrahedron element is more complex to calculate, because the blade flexures have a trapezoidal outline and therefore linear beam theory is not directly applicable. To approximate the lateral stiffness of blade flexure  $ab$ , we take the average stiffness of two beams, one with length  $L_{a_1b_1}$  and one with  $L_{a_3b_3}$ , as indicated in Fig. 4. In this way, the equivalent stiffness for the wire flexure  $K_b$  is approximated as:

$$K_b = \left[ \frac{4}{3EI/L_{a_1b_1}^3 + 3EI/L_{a_3b_3}^3} + \frac{24}{5GA/L_{a_1b_1} + 5GA/L_{a_3b_3}} \right]^{-1}, \quad (3)$$

where

$$L_{a_1b_1} = \sqrt{L_{a_1c_1}^2 / 4 + S_y^2} \quad (4)$$

and

$$L_{a_3b_3} = \frac{P_z - S_z}{P_z} L_{a_1b_1}. \quad (5)$$

The thickness in the blade flexures of the tetrahedron varies linearly in the z-direction, indicated by  $t_{max}$  and  $t_{min}$  in Fig. 4a. The thickness changes proportionally with the length of the line segments of the top triangle  $a_1b_1c_1$  and the bottom triangle  $a_3b_3c_3$ . This is to make sure that the bending stresses due to displacement in the motion direction have an even distribution in the z-direction of the element. This means that:

$$t_{max} = \frac{P_z}{P_z - S_z} t_{min}. \quad (6)$$

We approximate the height of the blade flexures by  $S_z$ , which is the height of the total tetrahedron excluding the rigid bar in Fig. 4a. The cross-sectional area in equation (3) is then:

$$A = (t_{min} + t_{max})S_z / 2. \quad (7)$$

Note that we approximate the shear deformation in equation (3) by using the shear constant for a rectangular cross section. The moment of inertia  $I$  for the trapezoidal cross-section is given by Ref. [15] as:

$$I = \frac{S_z^3 (t_{min}^2 + 4 t_{min} t_{max} + t_{max}^2)}{36(t_{min} + t_{max})}, \quad (8)$$

where we also approximate the height of the blade flexures by  $S_z$ .

### 3.4. Constraint stiffness terms of the prism element

In this section we derive analytic expressions for the stiffness of the end effector (edge  $c_1c_3$ ) in the four constraining directions of the prism element illustrated in Fig. 4b, using its equivalent representation. Throughout the following sections we use linear beam equations to calculate the stiffness of the blade flexures, which can be found in for example [15,16]. We neglect the stiffness in the free (low-stiffness) directions of the blade and wire flexures.

We start with  $K_{\theta_x}$ , which is the rotational stiffness of edge  $c_1c_3$  around the x-axis as illustrated in Fig. 8b. For this we apply a moment  $M_{ext}$  around the x-axis, determine the reactions on the blade and wire flexure, compute their corresponding displacements and from this determine the rotation around the x-axis. Fig. 10a shows the rigid part of the equivalent representation, in the yz-plane. The external moment  $M_{ext}$  is applied at edge  $c_1c_3$  and results in forces  $F_{cp}$  from the blade flexure, and  $F_{bp}$  from the wire flexure. Note that both the blade and the wire flexure are free to rotate around the x-axis and therefore cannot exert a moment in the yz-plane. The displacements  $\delta_{bp}$  and  $\delta_{cp}$  fully determine the rotation around

the x-axis, which means that the rotational stiffness can be written as:

$$K_{\theta_x} = \frac{M_{ext}}{\delta_{bp}S_y + \delta_{cp}S_y}. \quad (9)$$

What is left is to determine  $\delta_{bp}$  and  $\delta_{cp}$  as a result of  $M_{ext}$ . We start with  $\delta_{bp}$ . Static equilibrium in the yz-plane gives:

$$\delta_{bp} = \frac{F_{bp}}{K_{bp}} = \frac{M_{ext}/S_y}{K_{bp}}, \quad (10)$$

where  $K_{bp}$  is the equivalent stiffness of the wire flexure from equation (1). Displacement  $\delta_{cp}$  is more complex to calculate since  $M_{ext}$  not only results in a force  $F_{cp}$  on the blade flexure but also introduces a moment  $M_{cp}$ , as illustrated in 10b where the rigid part is shown in the xz-plane. This moment counteracts the displacement caused by the force  $F_{cp}$ . The total displacement can be calculated as:

$$\delta_{cp} = F_{cp} \left[ \frac{L_{a_2c_2}^3}{3EI_p} + \frac{6L_{a_2c_2}}{5Gth} \right] - M_{cp} \frac{L_{a_2c_2}}{2EI_p}, \quad (11)$$

where the first term is the displacement due to the force and the last term is the displacement due to the moment. Using the free-body diagrams in Fig. 10 it can be shown that  $M_{cp} = F_{cp}L_{a_2c_2}/2$  and  $F_{cp} = M_{ext}/S_y$ , which gives:

$$\delta_{cp} = \frac{M_{ext}}{S_y} \left[ \frac{L_{a_2c_2}^3}{12EI_p} + \frac{6L_{a_2c_2}}{5Gth} \right]. \quad (12)$$

Substituting equations (1), (10) and (12) in 9 and rearranging gives the stiffness around the x-axis as:

$$K_{\theta_x} = S_y^2 \left[ \frac{\frac{L_{a_2c_2}^3}{4} + L_{a_2b_2}^3 + L_{b_2c_2}^3 + \frac{6(L_{a_2c_2} + L_{a_3b_2} + L_{b_2c_2})}{5Gth}}{3EI_p} \right]^{-1}, \quad (13)$$

where  $L_{a_2b_2} = L_{b_2c_2} = \sqrt{L_{a_2c_2}^2/4 + S_y^2}$ .

The stiffness terms in the other constraining directions of the prism element solely depend on blade flexure  $ac$ . This can be proven as follows, using the equivalent representation in Fig. 8b. If the wire flexure contributes to the stiffness, it causes a reaction force in the z-direction on the rigid part in point b. Moment equilibrium in the yz-plane can then not be satisfied, because the blade and wire flexure are free to rotate in this plane. Solely the stiffness  $K_{\theta_x}$  is dependent on the wire flexure, because in that case the external moment  $M_{ext}$  in Fig. 10a makes moment equilibrium possible. The translational stiffness in z-direction of edge  $c_1c_3$  is therefore simply equal to the lateral stiffness of blade flexure  $ac$  as:

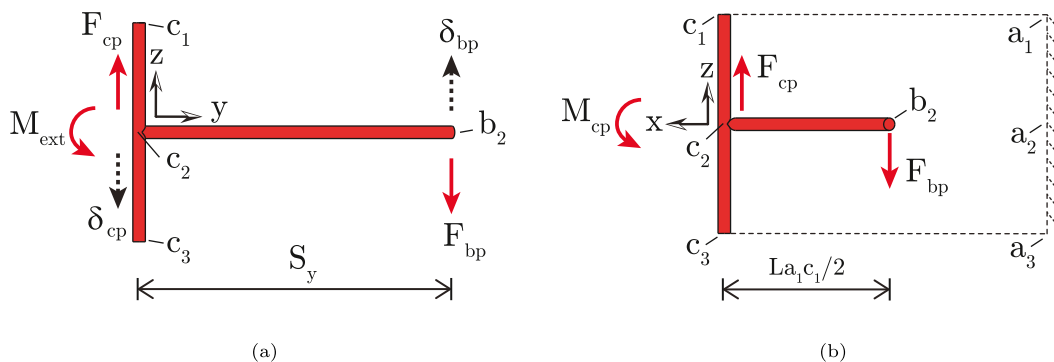


Fig. 10. Model for determining the rotational stiffness  $K_{\theta_x}$  around the x-axis of the prism of Fig. 4b by considering a moment  $M_{ext}$  at  $c_2$  on the rigid part of the equivalent representation, shown in the yz-plane (a) and xz-plane (b).

$$K_z = \left[ \frac{I_{a_2c_2}^3}{3EI_p} + \frac{6L_{a_2c_2}}{5Gth} \right]^{-1} \quad (14)$$

Using the same reasoning, a moment around the y-axis is solely counteracted by flexure  $ac$  and therefore the rotational stiffness around the y-axis is:

$$K_{\theta_y} = \frac{EI_p}{L_{a_2c_2}} \quad (15)$$

and finally the translational stiffness in x-direction is:

$$K_x = \frac{EtS_z}{L_{a_2c_2}} \quad (16)$$

### 3.5. Constraint stiffness terms of the tetrahedron element

In this section, we derive equations for the stiffness in the four constraining directions of the tetrahedron element, as illustrated in Fig. 4a. The procedure is similar to that of the prism, except that we approximate the stiffness of the flexures because of their trapezoidal shape. For simplicity, we assume that  $P_y = 0$  in Fig. 4a, such that blade flexure  $ac$  is vertical and coordinate system  $uvw$  aligns with system  $xyz$ .

We start with the translational stiffness at point  $P$  in  $v$ -direction  $K_v$ , as illustrated in Fig. 4a. Consider the equivalent representation shown in Fig. 8a. The free-body diagram of the rigid part after application of a force  $F_{ext}$  at point  $P$  in the  $v$ -direction is shown in Fig. 11. The displacement of  $P$   $\delta_p$  in the  $v$ -direction is fully defined by the displacements  $\delta_b$  and  $\delta_c$ . Because the deformations are small, we can calculate the contributions of the two displacements  $\delta_b$  and  $\delta_c$  to the displacement of  $P$  separately and then add them [16]. We start with the contribution of  $\delta_b$ . Static equilibrium gives:

$$\frac{F_{ext}}{F_b} = \frac{S_y}{\sqrt{S_y^2 + P_z^2}} \quad (17)$$

The displacements are related by the reciprocal of this transmission ratio [3] as:

$$\frac{\delta_{p,b}}{\delta_b} = \frac{\sqrt{S_y^2 + P_z^2}}{S_y}, \quad (18)$$

where  $\delta_{p,b}$  is the displacement of  $P$  in  $v$ -direction due to the displacement  $\delta_b$ . The displacement of  $P$  in the  $v$ -direction as a result of displacement  $\delta_c$

can be derived in the same way as:

$$\frac{\delta_{p,c}}{\delta_c} = \frac{P_z}{S_y} \quad (19)$$

The stiffness  $K_v$  is the external force divided by the total displacement in  $v$ -direction of point  $P$ :

$$K_v = \frac{F_{ext}}{\delta_{p,c} + \delta_{p,b}} = \frac{F_{ext}}{\frac{P_z}{S_y}\delta_c + \frac{\sqrt{S_y^2 + P_z^2}}{S_y}\delta_b} \quad (20)$$

What remains is to find the displacements  $\delta_b$  and  $\delta_c$  due to force  $F_{ext}$ . The displacement  $\delta_b$  is simply the force  $F_b$  divided by the stiffness of the wire flexure:

$$\delta_b = \frac{F_b}{K_b} = \frac{\frac{\sqrt{S_y^2 + P_z^2}}{S_y}F_{ext}}{K_b}, \quad (21)$$

where  $K_b$  is the equivalent stiffness of the wire flexure from equation (3). The displacement  $\delta_c$  is computed in a similar way as for the prism element. The free-body diagram in Fig. 11b shows that, similar to the computation for the prism, a moment counteracts the displacement due to the force  $F_c$ . Note that  $F_{b,z}$ , the component of  $F_b$  in  $z$ -direction, is equal to  $F_c$ . This force acts on an arm which is half the length of blade flexure  $ac$ , and therefore the term between the brackets in equation (12) for the prism element can be used to compute the displacement  $\delta_c$ . However, because the blade flexures have a trapezoidal shape, we compute their average stiffness using the two lengths  $L_{a_1c_1}$  and  $L_{a_3c_3}$ , similar to the procedure for the equivalent wire flexure for the tetrahedron element in section 3.3. Noting that  $F_c = F_{ext}P_z/S_y$ , the displacement  $\delta_c$  is approximated as:

$$\delta_c = F_{ext} \frac{P_z}{S_y} \left[ \frac{2}{12EI/L_{a_1c_1}^3 + 12EI/L_{a_3c_3}^3} + \frac{12}{5GA/L_{a_1c_1} + 5GA/L_{a_3c_3}} \right], \quad (22)$$

where

$$L_{a_3c_3} = \frac{P_z - S_z}{P_z} L_{a_1c_1}. \quad (23)$$

Substituting equations (3), (21) and (22) in 20 yields the stiffness  $K_v$  in  $v$ -direction at point  $P$ :

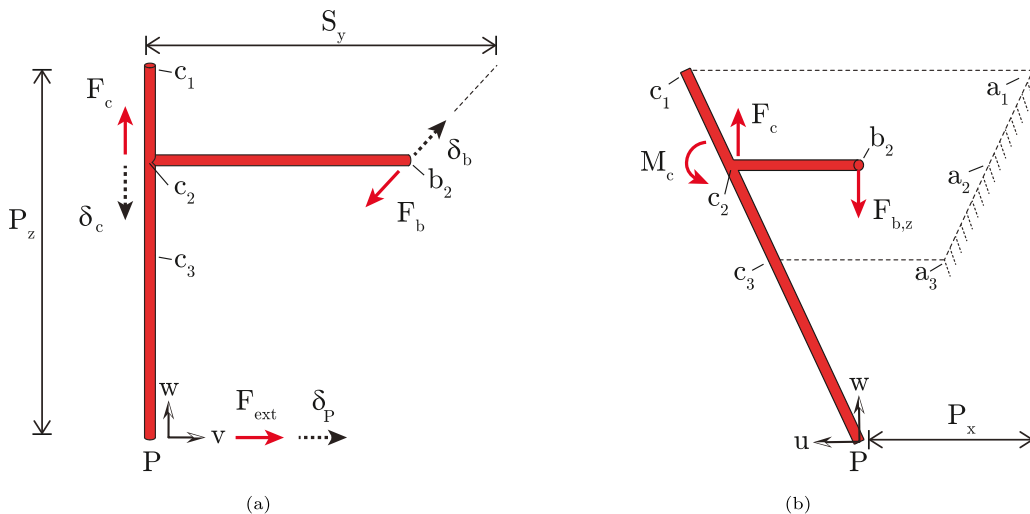


Fig. 11. Model for determining the translation stiffness  $K_v$  in point  $P$  of the tetrahedron element in Fig. 4a by considering a force  $F_{ext}$  on the rigid part of the equivalent representation, shown in the  $vw$ -plane (a) and  $uw$ -plane (b).

$$K_v = S_y^2 \left[ \frac{2P_z^2}{12EI/L_{a_1c_1}^3 + 12EI/L_{a_3c_3}^3} + \frac{12P_z^2}{5GA/L_{a_1c_1} + 5GA/L_{a_3c_3}} + \frac{4(S_y^2 + P_z^2)}{3EI/L_{a_1b_1}^3 + 3EI/L_{a_3b_3}^3} + \frac{24(S_y^2 + P_z^2)}{5GA/L_{a_1b_1} + 5GA/L_{a_3b_3}} \right]^{-1} \quad (24)$$

The stiffness in the other three constraining directions of the tetrahedron element solely depend on blade flexure *ac*. This is because a reaction force in the wire flexure has a *v*-component in the *v*-direction, which is not counteracted by the blade flexure because it is free in that direction. Therefore, the wire flexure is only active in the case of a force at *P* with a component in the *v*-direction, which means that solely constraint stiffness  $K_v$  depends on the wire flexure.

To compute the translation stiffness in the *w*-direction  $K_w$ , consider a force at *P* in the *w*-direction on the equivalent representation in Fig. 11b. This force will induce a force and a moment at edge  $c_1c_3$  on blade flexure *ac*, which counteracts its displacement in the same way as when computing equation (22). Because again the moment arm of the force is half of the length of blade flexure *ac*, we can simply use the terms in brackets in equation (22):

$$K_w = \left[ \frac{2}{12EI/L_{a_1c_1}^3 + 12EI/L_{a_3c_3}^3} + \frac{12}{5GA/L_{a_1c_1} + 5GA/L_{a_3c_3}} \right]^{-1} \quad (25)$$

To compute the stiffness in the *u*-direction  $K_u$ , consider the *uw*-view of the equivalent representation in Fig. 11b. The stiffness  $K_u$  is dependent on the axial deformation of blade flexure *ac* and the torsional stiffness around its *v*-axis with moment arm  $P_z - S_z/2$  as:

$$K_u = \left[ \frac{L_{a_2c_2}}{EA} + \frac{(P_z - S_z/2)^2 L_{a_2c_2}}{EI} \right]^{-1} \quad (26)$$

where we approximate the length of blade flexure *ab* using  $L_{a_2c_2} = (L_{a_1c_1} + L_{a_3c_3})/2$ . Similarly, the rotational stiffness  $K_{\theta_v}$  is:

$$K_{\theta_v} = EI/L_{a_2c_2} \quad (27)$$

### 3.6. Comparison of the equations to finite-element simulations

In this section we compare the stiffness equations to simulations with the finite-element modeling (FEM) software package Comsol. For this we define a ‘standard design’ for both the tetrahedron and prism element. As a second test, we vary the design parameters one-by-one from this standard design and compare the effect on the stiffness change using graphs and an error metric.

The dimensions and material parameters chosen for the standard design of the tetrahedron and prism element are listed in Table 1. The dimensions are chosen such that the standard design is roughly similar to the elements used in the four joint designs in section 2. The tetrahedron and prism elements as shown in Fig. 4 were modeled in Comsol using shell elements. Edge  $a_1a_3$  is fixed and the end effector (edge  $c_1c_3$ ) is defined as rigid using the ‘rigid connector’ option. In the tetrahedron element, this rigid edge is extended to reach point *P*. The results for the prism and tetrahedron element are listed in Tables 2 and 3 respectively, together with their relative error.

As a second test, the parameters from the standard design are varied one-by-one and the stiffness terms  $K_{\theta_x}$  (for the prism) and  $K_v$  (for the tetrahedron) are compared to finite-element simulations. These two particular stiffness terms are chosen because they are dependent on all three blade flexures. The results for the prism are shown in Fig. 12. The design parameters range from a fifth of their standard value to five times their standard value. This is expected to be large enough to cover most practical uses. The results for the tetrahedron element are listed in Fig. 13. The parameters are again changed to one-fifth and five times the standard value, with two exceptions. The height  $S_z$  has a maximum value

**Table 1**

Parameters of the chosen standard designs of the tetrahedron and prism element.

Variable	Tetrahedron	Prism
$L_{a_1c_1}$	50 [mm]	50 [mm]
$S_y$	50 [mm]	50 [mm]
$S_z$	25 [mm]	25 [mm]
$t_{min}$	0.5 [mm]	–
$t$	–	0.5 [mm]
$P_x$	25 [mm]	25 [mm]
$P_y$	0 [mm]	0 [mm]
$P_z$	50 [mm]	infinite
$E$	210 [GPa]	210 [GPa]
$G$	80 [GPa]	80 [GPa]

**Table 2**

Outcomes of the comparison for the prism, showing a small error between the equations and the finite-element model, for the standard design defined in Table 1.

Stiffness term	FEM	Equations	Error
$K_x$ [N/m]	5.32e7	5.25e7	1.36%
$K_y$ [N/m]	3.14e3	free	–
$K_z$ [N/m]	2.78e6	2.74e6	1.36%
$K_{\theta_x}$ [Nm/rad]	2.27e3	2.23e3	1.75%
$K_{\theta_y}$ [Nm/rad]	2.81e3	2.73e3	2.52%
$K_{\theta_z}$ [Nm/rad]	3.19e0	free	–

**Table 3**

Outcomes of the comparison for the tetrahedron, showing a larger error between the equations and the finite-element model, for the standard design defined in Table 1.

Stiffness term	FEM	Equations	Error
$K_u$ [N/m]	4.06e6	3.62e6	11.0%
$K_v$ [N/m]	2.87e6	2.38e6	16.9%
$K_w$ [N/m]	2.37e7	2.61e7	10.1%
$K_{\theta_u}$ [Nm/rad]	1.18e2	free	–
$K_{\theta_v}$ [Nm/rad]	5.90e3	5.27e3	10.7%
$K_{\theta_w}$ [Nm/rad]	1.98e1	free	–

of 40 mm, because larger values will (almost) close off the bottom of the element. For the same reason, the minimum value of  $P_z$  is chosen as 35 mm. The plots in Fig. 13e and f contain the same information but the latter has a log-scale for the y-axis.

To quantify the errors, a normalized mean absolute error (NMAE) is computed. The NMAE is a regular MAE normalized by the maximum value in the displacement range as:

$$NMAE = \frac{\frac{1}{N} \sum_{n=1}^N |\hat{y}_n - y_n|}{\max|y|} \quad (28)$$

in which *N* is the amount of measured data points (10 per design parameter),  $\hat{y}$  is the value from the equations and *y* is the data from the finite-element model.

The stiffness equations for the prism show a good correspondence with the finite-element simulations, with a maximum NMAE of 1.9%. The equations for the tetrahedron do capture the qualitative behavior but show significantly larger errors with a maximum NMAE of 34.9% in the case where the width  $S_y$  is varied. This is expected to be caused by the approximation of the trapezoidal blade flexures. Also, to compute the equivalent stiffness of blade flexures *ab* and *bc* in equation (3), the lateral stiffness of the blade flexures is used. This is correct in the case of the prism element because the force  $F_{bp}$  in Fig. 9 is perpendicular to the two blade flexures. For the tetrahedron element this is not the case. A continuum mechanics approach is expected to give better results in this situation.

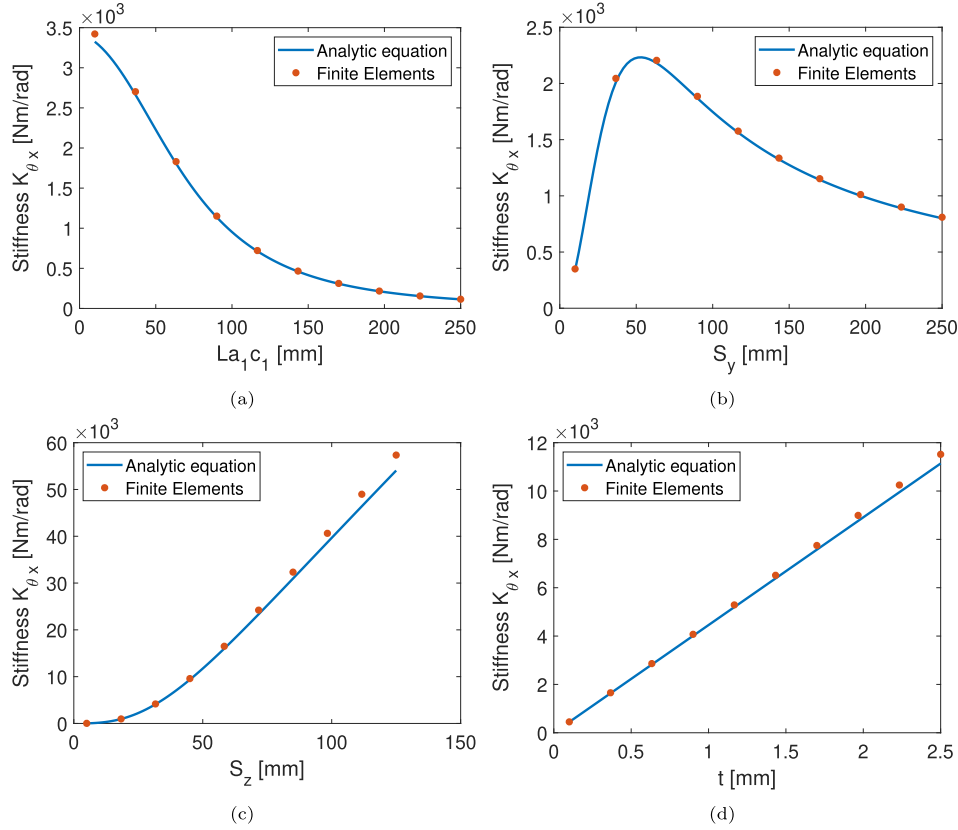


**Fig. 12.** Outcomes of the comparison of the analytic equation for stiffness  $K_{\theta_x}$  with finite-element simulations for the prism in Fig. 4b, showing a good correspondence with a NMAE of 1.9%. The design parameters are varied one-by-one from the standard design defined in Table 1.

The stiffness in the directions denoted as ‘free’ in Tables 3 and 2 are significantly lower than the stiffness in the other directions. This validates that these are the degrees of freedom of the elements, as was derived in section 3.2.

#### 4. Discussion

The prism element has an optimal width  $S_y$  for which the rotational stiffness  $K_{\theta_x}$  is highest. For the standard design this is the optimum in the graph in Fig. 12b. A larger width  $S_y$  results in a larger moment arm of the equivalent wire flexure (representing blade flexures  $ab$  and  $bc$ ) which increases stiffness  $K_{\theta_x}$ , but it also results in longer blade flexures  $ab$  and  $bc$  which decreases stiffness  $K_{\theta_x}$ . The optimal width  $S_{y,opt.}$  can be calculated by first setting the derivative of  $K_{\theta_x}$  with respect to  $S_y$  to zero as:

$$\frac{\partial K_{\theta_x}(S_y)}{\partial S_y} = 0. \tag{29}$$

Solving for  $S_y$  gives the optimal width  $S_{y,opt.}$  as:

$$S_{y,opt.} = \frac{1}{2} \left[ \sqrt{4 L_{a_2c_2}^4 + \frac{48 L_{a_2c_2}^2 S_z^2 (\nu + 1)}{5}} + L_{a_2c_2}^2 + \frac{12 S_z^2 (\nu + 1)}{5} \right]^{\frac{1}{2}}, \tag{30}$$

where  $\nu$  is Poisson’s ratio  $\nu = 2G/E - 1$ . The graph in Fig. 12b shows that the width  $S_y$  of 50 mm of the standard design is close to its optimal value. Table 2 shows that for the standard design, stiffness terms  $K_{\theta_x}$  and  $K_{\theta_y}$  are of comparable magnitude.

The insights from the analysis of the isolated tetrahedron and prism elements can be used when designing complete joints consisting of

multiple elements in series. For example, it is useful to know that the rotational stiffness terms  $K_{\theta_x}$  and  $K_{\theta_y}$  are of comparable magnitude for the standard prism design. If one of these stiffness terms would be much lower, the joint should be designed such that a large moment arm between the end effector and such a low-stiffness rotation axis are avoided. Note that equations for coupling terms are not derived, which are needed for a full analysis of the stiffness at the end effector of a serial chain of elements. These could be derived using the procedure in this paper, but will result in lengthy equations. In this case, a numerical optimization is expected to be more useful.

Because of the specific shape of the tetrahedron element it can be connected in series without intermediate bodies, which is new with respect to the designs currently found in literature. Edges  $a_1a_3$  and  $c_1c_3$  of the tetrahedron in Fig. 4a form the interfaces at which other elements can be connected. If two tetrahedron elements are connected such that their connecting edges and corresponding vertices coincide (as in the two presented spherical joint designs), no intermediate bodies are needed. Connecting elements in series helps to increase the range of motion, because the strains due to displacement in the motion direction of the joint are distributed over the elements [17,18]. The state-of-the-art designs two, three and four shown in Fig. 1 could also be connected in series to increase their range of motion, if the joints are redesigned such that their rotation points coincide. However, this results in intermediate bodies which increase build volume, weight and material usage, and often deteriorate dynamic performance due to uncontrolled vibrations [1,13].

In [18], a distinction is made between flexure systems and flexure elements, of which the first type possesses rigid bodies and the latter does not. In this perspective, the designs presented in this paper are considered as a flexure element rather than a flexure system.

The Tetra II design shown in Fig. 5 could be fabricated using Wire Electrical Discharge Machining (WEDM), instead of using additive

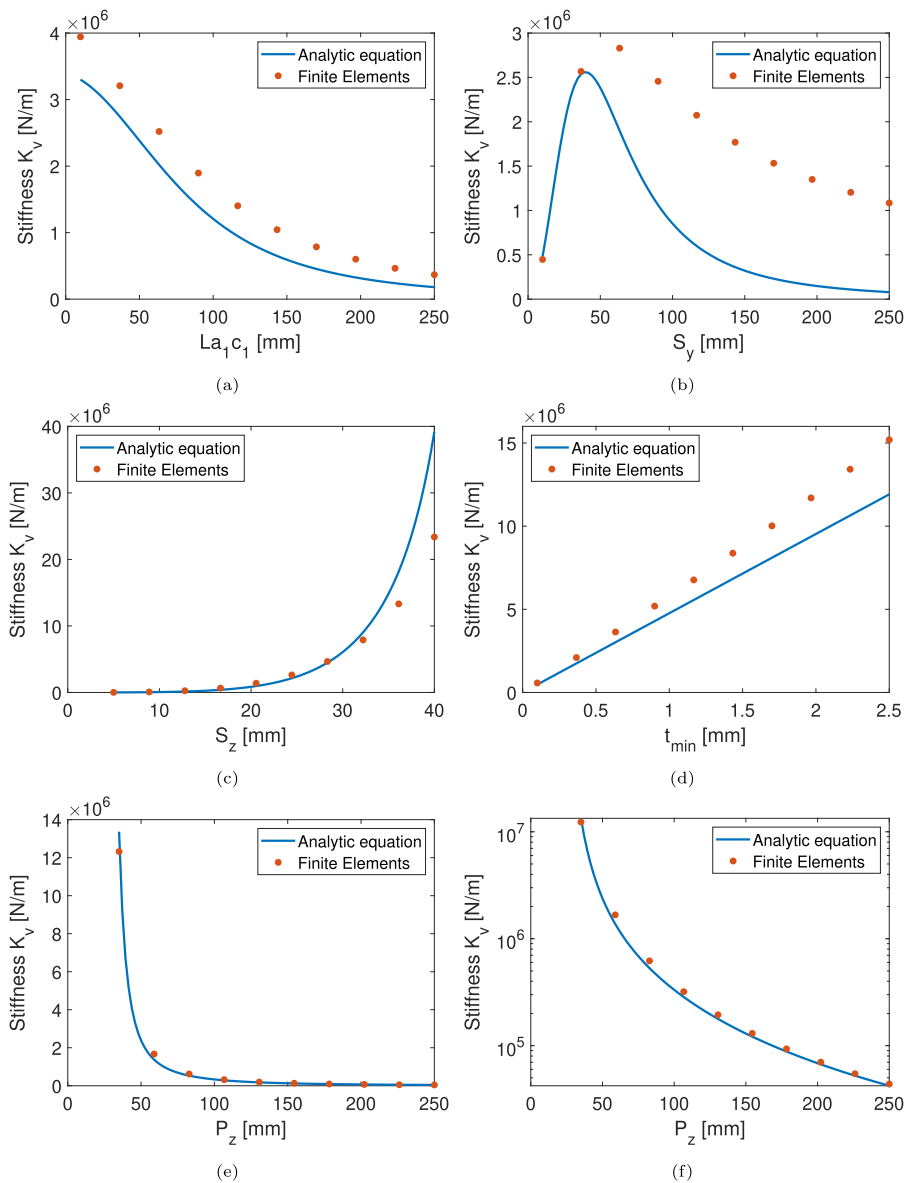


Fig. 13. Outcomes of the comparison of the analytic equation for stiffness  $K_v$  with finite-element simulations for the tetrahedron in Fig. 4a, showing that only the qualitative behavior is captured with a NMAE of 34.9%. Graph f) shows the same data as graph e) but uses a log scale for the y-axis.

manufacturing of titanium as in the demonstration movie that can be found online using the DOI of this article. WEDM is a proven technique for the fabrication of flexure mechanisms and angles of  $45^\circ$  are feasible.

### 5. Conclusion

In this paper we have presented designs of two spherical flexure joints named Tetra I and Tetra II, together with their derived planar versions. The designs are formed by tetrahedron-shaped elements, each composed of three blade flexures with a trapezoidal shape, that are connected in series without intermediate bodies. This is new with respect to the designs currently found in literature and helps to increase the range of motion. The Tetra I design consists of two arms, each built up from four tetrahedron elements in series. The Tetra II design consists of three tetrahedron elements which are also connected in series, but form a nested configuration.

We showed that the tetrahedron element is a generalized version of the triangular prism from earlier work. The tetrahedron changes into a triangular prism in the special case where the rotation point of the

spherical joints is chosen at infinity.

We developed equivalent representations of the tetrahedron and prism elements consisting of a blade flexure and a wire flexure connected by a rigid part. Using these representations we have proven that three of the four constraint stiffness terms solely depend on the properties of the main blade flexure.

From the equivalent representations we derived equations for the constraint stiffness terms for both the prism and the tetrahedron, resulting also in an equation for the optimal width for which the prism has the highest rotational stiffness along the torsion axis of the main blade flexure.

By comparing the analytic equations to finite-element simulations, a good correspondence for the prism was found with a normalized mean squared error (NMAE) of 1.9%. For the tetrahedron element, the equations showed to only capture the qualitative behaviour with a NMAE of 34.9%, which is expected to be caused by the approximation of the trapezoidal blade flexures.

### Declaration of competing interest

The authors declare that they have no known competing financial interests or personal relationships that could have appeared to influence the work reported in this paper.

### Acknowledgment

This work is part of the research programme Möbius with project number 14665, which is (partly) financed by the Netherlands Organisation for Scientific Research (NWO).

### Appendix A. Supplementary data

Supplementary data to this article can be found online at <https://doi.org/10.1016/j.precisioneng.2021.03.002>.

### References

- [1] Naves M, Aarts R, Brouwer D. Large stroke high off-axis stiffness three degree of freedom spherical flexure joint. *Precis Eng* 2019;56:422–31.
- [2] Lobontiu N, Paine JS. Design of circular cross-section corner-filletted flexure hinges for three-dimensional compliant mechanisms. *J Mech Des* 2002;124(3):479–84.
- [3] Soemers H. *Design Principles for precision mechanisms*. T-Pointprint; 2011.
- [4] Howell LL, Magleby SP, Olsen BM. *Handbook of compliant mechanisms*. John Wiley & Sons; 2013.
- [5] Trease BP, Moon Y-M, Kota S. Design of large-displacement compliant joints. *J Mech Des* 2005;127(4):788–98.
- [6] Brecher C, Pyschny N, Behrens J. Flexure-based 6-axis alignment module for automated laser assembly. In: *International precision assembly seminar*. Springer; 2010. p. 159–66.
- [7] Schellekens P, Rosielle N, Vermeulen H, Vermeulen M, Wetzels S, Pril W. Design for precision: current status and trends. *Cirp Annals* 1998;47(2):557–86.
- [8] Rommers J, Naves M, Brouwer D, Herder J. A large range spatial linear guide with torsion reinforcement structures. In: *International design engineering technical conferences and computers and information in engineering conference*, vol. 51807. American Society of Mechanical Engineers; 2018.
- [9] D. Wiersma, S. Boer, R. Aarts, D. Brouwer, Design and performance optimization of large stroke spatial flexures, *J Comput Nonlinear Dynam* 9 (1). doi:10.1115/1.4025669.
- [10] M. Naves, D. Brouwer, R. Aarts, Building block-based spatial topology synthesis method for large-stroke flexure hinges, *J Mech Robot* 9 (4). doi:10.1115/1.4036223.
- [11] Hale LC. *Principles and techniques for designing precision machines*, Tech. rep. Livermore, CA (United States): Lawrence Livermore National Lab.(LLNL); 1999.
- [12] Blanding DL. *Exact constraint: machine design using kinematic principles*. American Society of Mechanical Engineers; 1999.
- [13] J. B. Hopkins, A visualization approach for analyzing and synthesizing serial flexure elements, *J Mech Robot* 7 (3).
- [14] Hopkins JB, Culpepper ML. Synthesis of multi-degree of freedom, parallel flexure system concepts via freedom and constraint topology (fact)–part i: Principles. *Precis Eng* 2010;34(2):259–70.
- [15] Gere J. *Mechanics of materials*. sixth ed. Brooks/Cole-Thomas Learning; 2004.
- [16] Hibbeler R. *Mechanics of materials*. Prentice Hall; 2005.
- [17] Merriam EG, Lund JM, Howell LL. Compound joints: behavior and benefits of flexure arrays. *Precis Eng* 2016;45:79–89.
- [18] Hopkins J. Designing hybrid flexure systems and elements using freedom and constraint topologies. *Mechanical Sciences* 2013;4(2):319–31.